Canted Current Sheet Mass Leakage and its Impact on Pulsed Plasma Thruster Performance[*]

J.W. Berkery[†] and E.Y. Choueiri[‡]

Electric Propulsion and Plasma Dynamics Laboratory (EPPDyL)
Mechanical and Aerospace Engineering Department
Princeton University, Princeton, New Jersey 08544

An analytical model of the leakage of the current sheet in a parallel plate pulsed electromagnetic accelerator is proposed and measurements of the velocity, electron number density, and impulse of the current sheet are presented. The theoretical and experimental results are compared to gain insight on the impact of plasma leakage on the impulse of the device. Plasma leakage is due to a fraction of propellant being forced under and past the current sheet due to the canting of the current sheet, which is a ubiquitous feature of such devices. The model uses a force balance to predict the current sheet velocity, and a mass balance to predict the mass of the current sheet and that of it plasma wake. The impulse resulting from the sheet and its wake is calculated and compared to momentum plate measurements. It is found that, with increasing propellant fill pressure, the wake impulse makes up an increasing percentage of the total impulse, indicating increasing plasma leakage. The impulse of the wake increases from about 10% to nearly 67% of the total impulse in argon discharges over the range of $75 - 400$ **mTorr**, and from 20% to 50% for neon. Although the impulse added by the plasma wake causes the total impulse to increase, the specific impulse and efficiency decrease. Overall, the plasma leakage phenomenon is detrimental to pulsed plasma thruster performance.

I. INTRODUCTION

In a parallel plate pulsed electromagnetic accelerator, two non-ideal behaviors have been observed: current sheet canting and plasma leakage. Figure 1 shows a photograph that illustrates these two features. The canting phenomenon has been explored in detail by Markusic et al [1–3]. Current sheet canting is the departure of the current sheet from a plane perpendicular to the electrodes to a plane that is skewed. The anode attachment always leads the cathode attachment, leading to a $j \times B$ force component that forces plasma towards the cathode, allowing for leakage.

After the canting angle has been established, the current sheet propagates with a constant canting angle, velocity and electron number density. Markusic et al's measurements clearly show the sheet maintains a constant canting angle [3]. Detailed magnetic field mapping and photography have shown that the velocity of the sheet stays constant as well [4]. The density of the sheet remaining constant is the least verified assumption. A detailed electron density mapping of an argon discharge at 100 mTorr [5] shows that the assumption is good at least in that case. Other, less detailed, electron density measurements made by the authors indicate that this assumption holds for other conditions as well, although Markusic showed that in some cases the peak electron number density actually *decreases* as the sheet propagates [1].

It is clear that leakage of plasma along the cathode could lead to a loss of momentum of that portion of the propellant. This should have a negative effect on the performance of the device. Although researchers have seen current sheet leakage in the past [6–8], a study of its effect on the impulse of the thruster has never been performed. Also, knowledge of the fundamental physics behind the leakage phenomenon
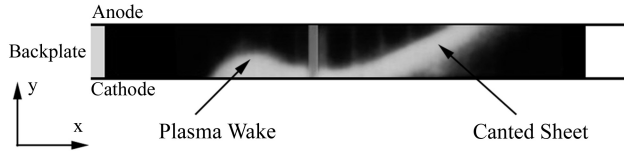
FIG. 1: Photograph of a discharge from [1], showing two non-idealities of current sheet behavior. The top electrode is the anode and the bottom electrode is the cathode. The plasma is moving from left to right. The ideal behavior would be for the current sheet to be perpendicular to the electrodes. Instead we see a canted sheet and a plasma wake trailing the sheet along the cathode. The vertical bar in the middle of the photograph is a physical structure that obscured the light, not a plasma structure.

and the partitioning of momentum into the sheet and wake was lacking. It is these questions that the current study will investigate, and aims to answer.

We have developed an analytical model to explain the observed behavior of the current sheet and plasma wake and to make predictions about quantities that have not been measured. We have chosen to avoid the use of computer simulations in favor of an analytical approach which has the promise of giving more accessible, albeit less detailed, insight. We will use a mass balance of ions in the current sheet to predict the mass of the sheet and a force balance to predict its velocity. The mass and velocity of the wake will also be predicted, and the subsequent predicted impulses will be compared to experimental data. These data include velocity, electron number density, and total impulse measurements. The measurements are made for argon and neon discharges over a range of initial propellant pressures, all at the same discharge energy.

II.   EXPERIMENTAL DATA

The device used in this study is the same as that used by Markusic et al in their current sheet canting studies [1–3]. The accelerator is not an actual thruster, but rather an idealized parallel plate accelerator with Pyrex sidewalls that allow good optical access to the discharge. The anode and cathode are made of copper and the area of the acceleration region measures 60 cm long and 10 cm wide, with a gap of 5 cm between the plates. The initial propellant distribution was a uniform gas fill. A pulse forming network was used to supply a current pulse with an approximately constant current for 25 μs.
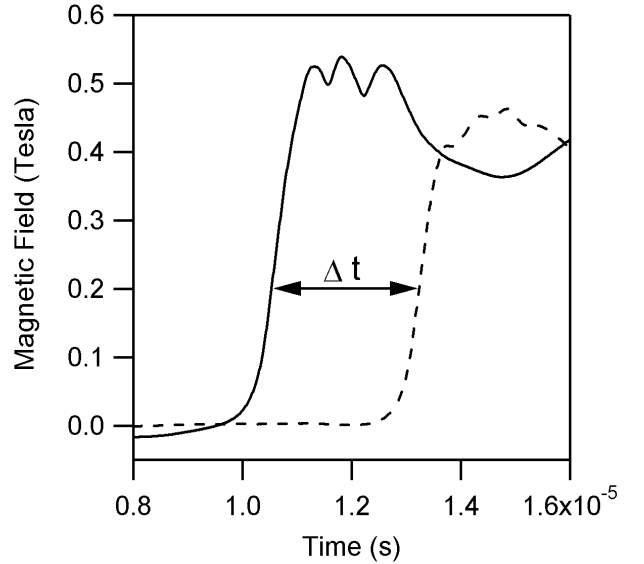

FIG. 2: The time-of-flight technique for measuring current sheet velocity from magnetic field measurements. This plot shows two measurements made 10 cm apart in an argon discharge at 75 mTorr.

Several experiments have been performed on this device which are relevant as points of comparison for an analytical model of the impulse of the device. We used a laser interferometer to measure the electron number density in the current sheet and magnetic field probes to measure its velocity. Together these measurements provide us with estimates of the sheet mass and impulse. We have also constructed a momentum plate, or ballistic pendulum, to measure the total impulse of the device. Each of these measurements will be described in detail.

A.   Sheet Velocity Measurements

The velocity of the current sheet is an important parameter for determining the performance of the accelerator. One reliable way to measure the velocity of the sheet is through the time-of-flight technique, using B-dot probes. Two probes are employed, separated by a known distance, and that distance is divided by the difference in arrival time of the sheet at the two probes. The arrival of the sheet is taken as the time at which the magnetic field rises to 0.2 Tesla (see figure 2). In the measurements presented here, the two B-dot probes were placed at distances of 35.5 cm and 45.5 cm from the backplate to accommodate sheet velocities on the order of 10^4 m/s.
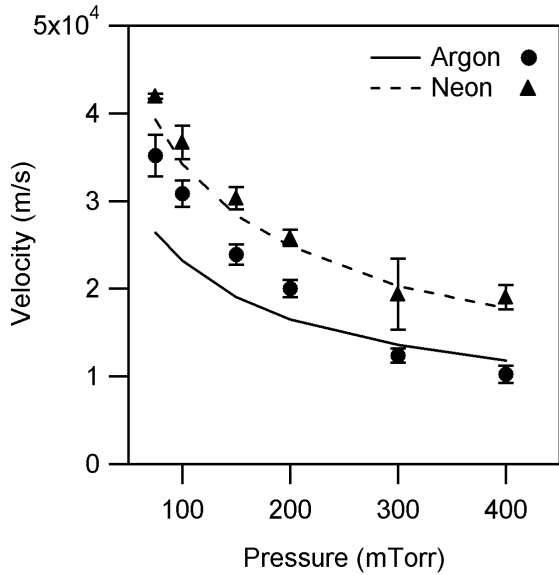
2

FIG. 3: The measured sheet velocities of argon and neon for a range of pressures. The measurements are compared to the predicted snowplow velocities, discussed in section III A.
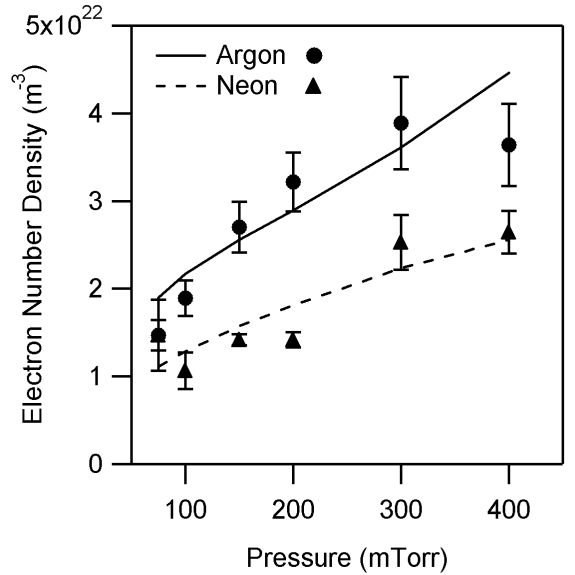
FIG. 4: The measured peak electron number densities in the sheet for argon and neon for a range of pressures, compared to the predicted ion densities from the model, discussed in section III B.

Figure 3 shows the sheet velocity measured in this way for argon and neon, compared to the snowplow velocity. The snowplow velocity will be described in further detail in the model section.

B.   Sheet Electron Number Density Measurements

With a few assumptions, electron density measurements in the current sheet will allow us to estimate the sheet mass and therefore the impulse. In this subsection we will present the electron number density measurements themselves. In the next subsection we use these measurements to determine the sheet mass.

We used a previously described [9] laser interferometer system to measure a representative peak electron number density in the sheet under different conditions. This system can measure the electron number density to within an accuracy of about ±12%.

We have seen from previous measurements that the density is not constant in the sheet, it increases from anode to cathode. For consistency we select points near the middle of the electrode gap as a basis of comparison. Also, while the interferometry measurement is time-resolved (i.e., the density rises and falls in the sheet), we display only the peak electron

number densities in figure 4. The data presented here are from measurements at a single location in the thruster, corresponding to the laser interferometer beam positioned in the middle of the electrode gap, at 38 cm from the backplate.

C.   Sheet Mass

The mass of the current sheet can be determined from the time-resolved electron density measurement. First, we will assume that the plasma in the sheet is singly ionized, therefore the electron number density is equal to the ion number density. Second, we can assume that the sheet is fully ionized, so that ions make up the entire mass of the sheet. This assumption is justified in section VI.

The total mass of the sheet ions, then, is the density integrated over the volume,

$$m_{sh} = \int \rho_i dV = \int \int \int m_i n_e dx dy dz. \quad (1)$$

In our experiment, the sheet is uniform in the z direction (out of the page in figure 1) therefore the dz term immediately comes out of the integral as d, the "depth" of the electrodes. In the y direction, the plasma density is not uniform. However, we have seen from a detailed map of the number density for
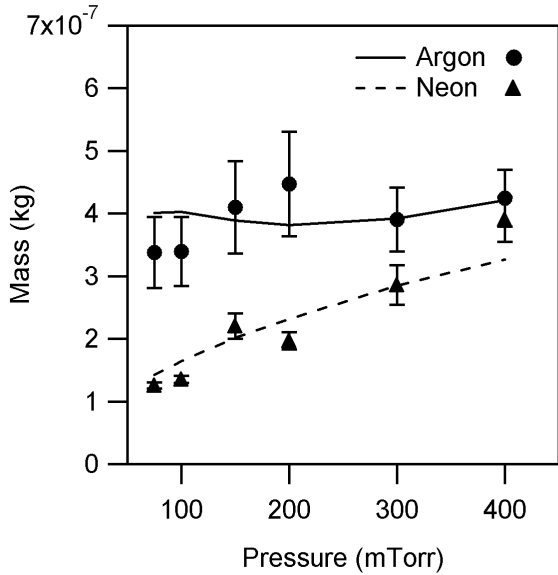
3

FIG. 5: The measured mass of the ions in the sheet for argon and neon for a range of pressures, compared to the values predicted by the model, discussed in section III B.
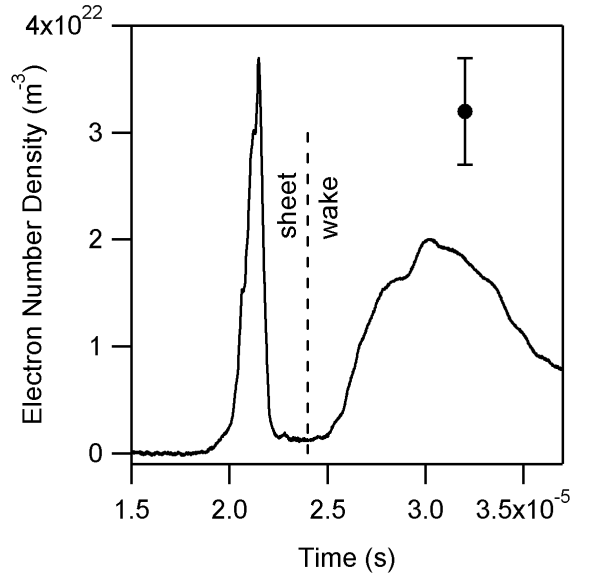

FIG. 6: Measurement of electron number density vs. time for argon, 300 mTorr, 9kV. The first peak is the sheet and the second peak is the wake. A typical error bar is also shown.

argon at 100 mTorr, that there is a linear increase in the electron number density from the cathode to the anode. Therefore measuring electron number density at the middle of the electrode gap and multiplying by the height of the sheet is equivalent to taking an average. Taking into account the canting of the sheet (which adds to the volume) the dy term becomes simply $h/cos\theta$.

The electron number density has been measured at a given point in x, with time resolution. This can easily be turned into a spatially resolved measurement in x by multiplying by the velocity, which is known. Therefore the expression for the sheet mass becomes

$$m_{sh} = \frac{m_i h d}{cos\theta} \int n_e v_{sh} dt. \qquad (2)$$

Care must be taken, however, to integrate only across the sheet, and not the wake. The integration must be cut off, then, at a time after the sheet has passed, and before the wake has arrived. This is not always easy, due to the close proximity of the structures, but an obvious separation point is often apparent. Figure 6 shows an example of a interferometry trace showing the separation point between the sheet and wake densities. The error associated with the slight connection of the two structures (the density does not always go to zero between them) is small compared to the integrated mass of the entire

sheet ahead of that point.

The sheet mass was calculated in this way, from equation 2, the electron number density measurements of section II B, and the velocity measurements of section II A, for each propellant over the usual range of pressures ($75 - 400$ mTorr). These data are shown in figure 5.

It should be noted, again, that the laser beam is not positioned at the exit of the accelerator. However, since the velocity and electron number density do not change after the canted sheet has been fully established, the mass and impulse will remain the same.

D. Sheet Impulse

It is straightforward to find the impulse of the sheet ions by multiplying the mass of the sheet ions and velocity of the sheet together. This is, of course, the impulse only of the ions in the sheet, neutrals will add some mass and thus impulse as well. The measured impulse of the sheet ions is shown in figure 7.
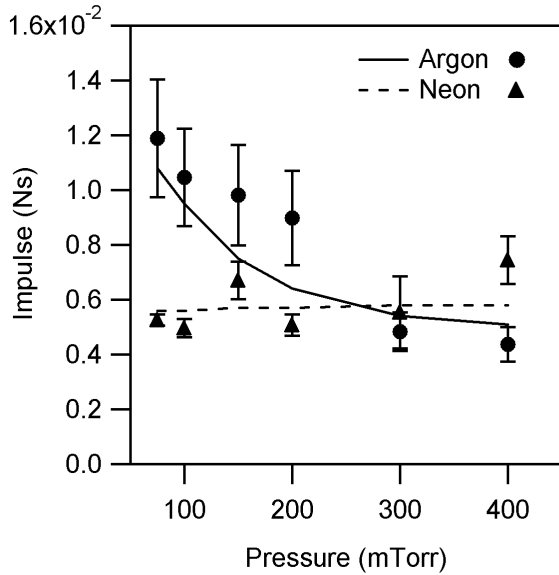
4

FIG. 7: The measured impulse of the ions in the sheet for argon and neon for a range of pressures, compared to the values predicted by the model, discussed in section III B.

E. Total Impulse

The total impulse of the device is the impulse supplied by the sheet and wake. A momentum plate was constructed to measure the impulse of the discharge and is shown in figure 8. Also known as a ballistic pendulum, the momentum plate is a method of measuring thrust or impulse of a thruster when a thrust stand cannot be used. Although a momentum plate is not as reliable as a thrust stand, in our case it was the most convenient way to measure impulse, as the accelerator was built for good optical access and a low inductance connection to the pulse forming network and cannot be mounted on a thrust stand. Momentum plates of various designs have been used by researchers in the past to measure the impulse of pulsed plasmas [10–16].

The momentum plate is a simple device. A flat plate attached to a pendulum arm is placed in front of the accelerator device. When the plasma discharge hits the plate, it imparts its momentum to the plate. This momentum is measured by measuring the plate's response. The motion of the plate is compared to its motion under a calibration, when it is struck with a known impulse.

For our measurements we constructed a plexiglass momentum plate that was 20 cm diameter. The plate was positioned a few cm away from the end of the electrodes. It was hung vertically on a pendu-
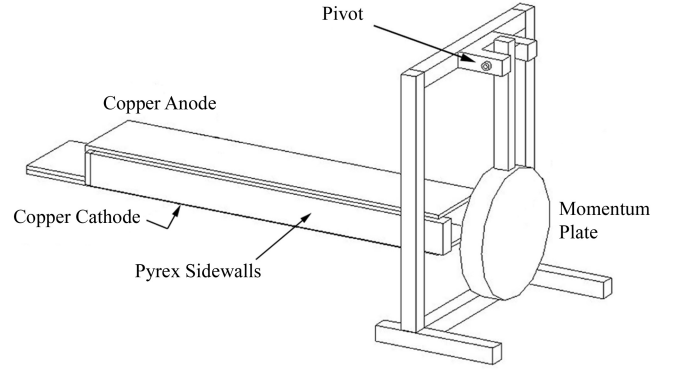

FIG. 8: Schematic of the accelerator and momentum plate.

lum arm of 28 cm length. The stainless steel ABEC-5 6085A bearings of the pendulum arm were selected to be as frictionless as possible to ensure a free swinging plate.

The plate, arm, and supporting structure were constructed out of plexiglass to avoid possible problems of arcing to the electrodes, or electromagnetic field influence on the plate motion. The plexiglass was able to handle the plasma impacts well, after many tens of shots there were no visible signs of erosion on the plate.

We measured the position of the plate with a laser positioning system. A laser beam was aimed at a mirror attached to the back side of the plate, and was deflected to a sensor placed outside of the vacuum tank. When the plate moved, the sensor recorded the beam movement as a voltage.

The calibration of the momentum plate was carried out by striking the plate with a test pendulum. The test pendulum included a Piezotronics pressure sensor on its tip. When the pressure sensor impacted the plate, the pressure vs. time signal was recorded, as well as the position vs. time of the swinging plate. To obtain the impulse of the test pendulum's impact, the pressure vs. time traces were integrated. The impact time of the test pendulum (and the plasma in the real experiments) was much less than the time scale of the swinging of the momentum plate, so the impact can be treated as instantaneous. By changing the starting angle of the test pendulum, we were able to test the momentum plate's response to a range of impulses. The calibration impulses were selected to be in the expected range of the impulse of the discharges $(0.01 - 0.02 \text{ Ns})$.

Measurements were repeated about ten times for each pressure for argon and neon. The total impulse measured with the momentum plate is shown in fig-
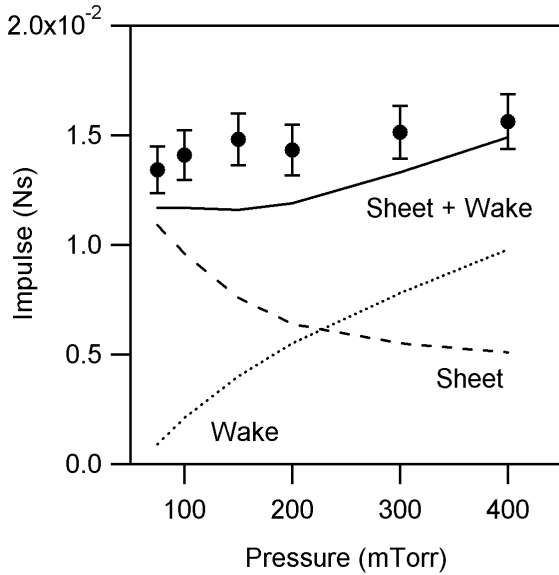
FIG. 9: The total impulse measurements made with the momentum plate for argon discharges from $75 - 400$ mTorr. Also shown on the plot are the model predictions for sheet, wake, and total impulse. These will be discussed further in section VI.
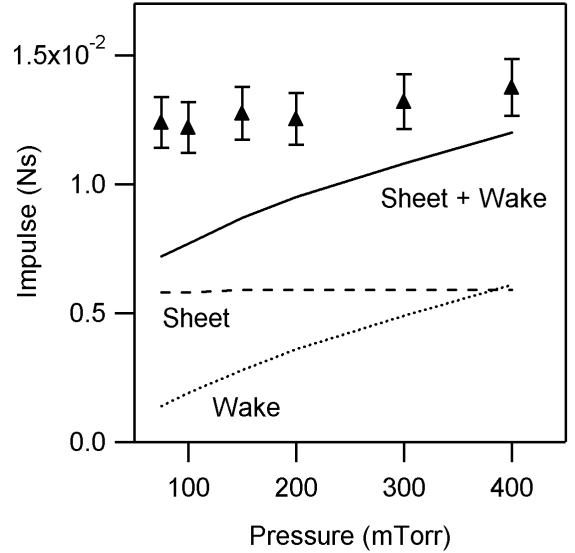

FIG. 10: The total impulse measurements made with the momentum plate for neon discharges from $75 - 400$ mTorr. Also shown on the plot are the model predictions for sheet, wake, and total impulse. These will be discussed further in section VI.

ure 9 for argon and figure 10 for neon.

III. DESCRIPTION OF THE MODEL

First, we will divide the development of the sheet into two processes: canting, and propagation. The goal of modelling the canting process is to understand the way that the sheet establishes itself into a canted structure. This problem has already been treated [2]. In this model, the sheet establishes itself into a fully canted structure and then maintains the same canting angle during the propagation phase. We will use Markusic's model to determine the canting angle of the sheet, which is a necessary input to the propagation model.

The model presented here will deal entirely with the propagation phase of the current sheet development. The goal of the model is to predict the constant velocity and mass of the sheet (thus the impulse of the sheet) and the final mass and velocity of the wake (and thus the total impulse of the plasma).

We will describe our analytical model in four sections: the sheet velocity, sheet mass, wake velocity, and wake mass. The most complicated section is predicting the sheet mass.

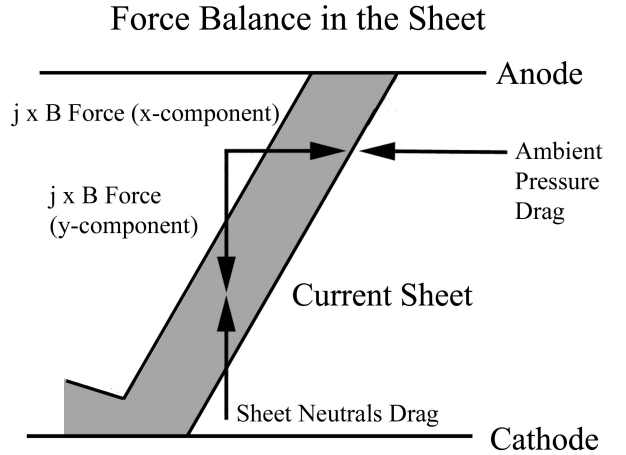FIG. 11: Diagram of the force balances performed to find the sheet velocity and the velocity of the ions towards the cathode in the sheet.

A. Sheet Velocity

The velocity that our measurements of sheet velocity are compared to in figure 3 is the snowplow velocity. The snowplow velocity is calculated from a balance between the force pushing the sheet and the opposing pressure drag of the ambient neutrals

6

ahead of the sheet. Figure 11 shows a diagram of the force balances in the x and y directions that will give us the velocity of the sheet and, later, the velocity of the ions towards the cathode. In the x direction, the force balance is,

$$\frac{1}{2}L'J^2 cos\theta = \frac{1}{2}\rho_a v_{sh}^2 (hd),\qquad(3)$$

where L' is the inductance per unit length of the device, J is the total current, θ is the canting angle, h is the inter-electrode distance, d is the width of the electrodes, and ρ_a is the ambient gas density. The force on the left hand side of the equation comes from the x-directed $j \times B$ force and Ampere's law (the inductance per unit length is a geometric factor that also includes μ_0 [17]).

Solving for the velocity, we find

$$v_{sp} = \sqrt{\frac{L'J^2 cos\theta}{hd\rho_a}}.\qquad(4)$$

B. Sheet Mass

The mass of the current sheet is more difficult to predict. Both ions and neutrals contribute to the mass and their densities in the sheet must be predicted. Although it is expected that ions make up the majority of the mass of the sheet, this is not known *a priori*.

For simplicity, we will consider the sheet to be of uniform density in both the x and y directions. Although the sheet clearly does not have a uniform density in the x direction, this approximation is necessary to simplify the model. Therefore we will consider the model current sheet to have a width equal to the full width at half maximum of the real sheet and an electron number density equal to the peak density of the real sheet. Figure 12 shows the model and real sheets.

The width of the sheet is necessary as an input to the model. We do not attempt to model the width, instead we will use experimental data. The effective width of the sheet used in the model is therefore obtained from experiments by the measured sheet mass divided by the product of the peak electron number density, the ion mass, and the sheet area:

$$w = \frac{m_{sh}}{n_e^{peak} m_i \frac{hd}{cos\theta}} = n_e^{peak}\int n_e v_{sh} dt.\qquad(5)$$
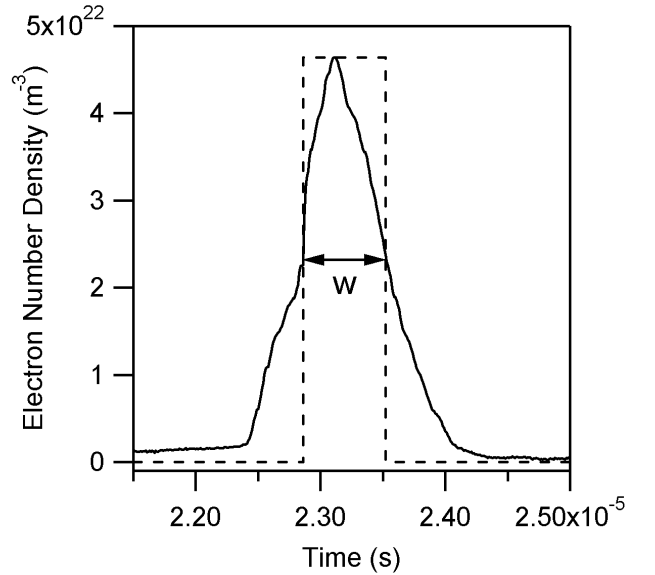

FIG. 12: Comparison of the density profile of the sheet in reality versus the approximation for the model.

Figure 13 shows the measured widths calculated in this way for argon and neon for a range of pressures from 75 to 400 mTorr. Also shown are the fits that are used as inputs to the model: for argon $w = 1 * 10^{-6}\text{s}*v_{sh}$ and for neon $w = .0357$ m. These widths, together with the measured current, gas properties, the geometry of the device, and electron temperature are the input parameters into the model of the current sheet mass. The electron temperature has been measured for an argon discharge at 100 mTorr [1], but not for neon. This issue will be discussed further in section VI.

The crux of the model is a mass balance. The rate of ions entering the sheet is balanced with the rate of ions leaving the sheet at the cathode as well as the creation and destruction of ions through ionization and recombination, respectively. These terms are displayed in figure 14. The ion mass balance equation is then written

$$\frac{dn_i}{dt} = 0 = R_i^e + R_{en}^{iz} - R_{ei}^{rc} - R_i^l.\qquad(6)$$

The convention for labelling rates, cross sections and frequencies that is followed here is that the subscript is for the particles involved and the superscript represents the process. The terms listed above are: the rate of ions entering the sheet, R_i^e, the rate of ionization in the sheet, R_{en}^{iz}, the rate of recombination in the sheet, R_{ei}^{rc}, and the rate of ions leaving the sheet, R_i^l. We have set this equation equal to
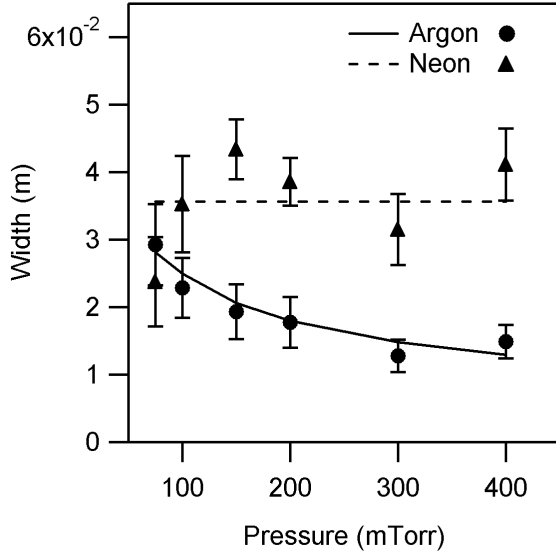
7

FIG. 13: Measured sheet widths, and the fits, shown as curves, that are used as inputs to the model for argon and neon from 75 to 400 mTorr.
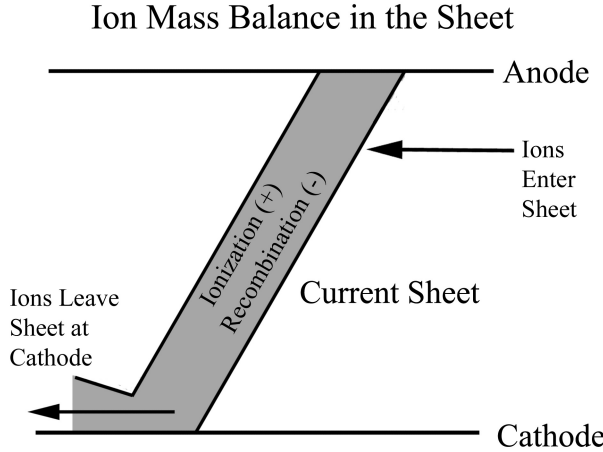
Ion Mass Balance in the Sheet

FIG. 14: Diagram of the mass balance for ions in the sheet. The mass balance is used to determine the ion number density in the sheet.

1. Ions Entering the Sheet

The sheet is moving into a volume of ambient neutrals with density n_a (the ambient neutrals are distinguished from the sheet neutrals with density n_n). In order for new ions to enter the sheet, these neutrals must be ionized as they are encountered. This may be accomplished in three ways: impact by thermal electrons, impact by directed ions (their directed energy due to the sheet velocity is much greater than their thermal energy), and photo-ionization.

The collisions that will result in a neutral entering the sheet un-ionized are momentum transfer collisions that accelerate the ambient neutrals up to sheet velocity. These are charge exchange and elastic scattering collisions.

In reality, the process of ionizing or accelerating ambient neutrals is a complex one. Ambient neutrals can be pre-ionized by photons from the plasma, fast electrons ahead of the sheet, and possibly by a shock wave [18]. We will make the simplifying approximation for our constant-density model sheet, that all of the ambient neutrals are ionized before or as they enter the sheet. Then the rate of ions entering the sheet is simply equal to the rate of ambient neutrals encountered:

$$R_i^e = n_a \frac{v_{sh}}{w} = n_a * \nu^{enc}. \tag{7}$$

where we have defined ν_a^{enc} as the frequency of ambient neutrals encountered by the sheet.

2. Ionization in the Sheet

Sheet neutrals, n_n, can be ionized in the sheet through collisions with thermal electrons or ions, or by photo-ionization. This is a rate of ion creation and a rate of neutral destruction,

$$R^{iz} = n_e \nu_{en}^{iz} = n_i \nu^{iz}. \tag{8}$$

3. Recombination in the Sheet

Ions and electrons in the sheet can recombine, creating neutrals while destroying ions. This can happen in two ways, through electron-electron-ion three-body recombination, or through radiative recombination:

$$R^{rc} = n_e \nu_{eei}^{tb} + n_e \nu_{ei}^{rr} = n_i \nu^{rc}. \tag{9}$$

zero because the ion number density in the sheet remains constant during the propagation phase. Each rate term will now be explained in turn.

8

4. Ions Lost to the Cathode

The presence of a plasma wake of significant density in these discharges implies that a significant loss of ions to the cathode is present. The loss rate of ions is given by

$$R_i^l = n_i \frac{v_y}{h} = n_i \nu^l. \tag{10}$$

We must now define v_y, the velocity of the ions towards the cathode. If we make an approximation that half of the current is carried by the ions, then we can define v_y as

$$v_y = \frac{\frac{1}{2}J}{edwn_i}, \tag{11}$$

where J is the total current, e is the electric charge, d is the depth of the electrodes in the z direction, and w is the width of the sheet. The current at the anode is purely electron current, and several researchers have made the assumption of purely ion current at the cathode in the past [7, 19]. For our idealized model sheet, the ion density is representative of the value in the middle of the electrode gap and the velocity of ions towards the cathode, v_y is a representative value as well, therefore the assumption of the current being divided between the ions and electrons in the center of the electrode gap is justified.

The velocity of the ions towards the cathode can also be defined, however, by a force balance in the sheet. This is similar to the force balance between the sheet and the ambient neutrals that gave us the sheet velocity (refer to figure 11). In this case we have a force on the ions due to the canted $j \times B$ force that is greater than the force due to the electric field. This force is opposed by the drag on the ions due to momentum transfer collisions with neutrals. Thus

$$\frac{1}{2}L'J^2 sin\theta = M_i v_y \nu_{in}^{mt} = m_i n_i \frac{hdw}{cos\theta} n_n v_y^2 Q_{in}^{mt}. \tag{12}$$

Therefore, together with equation 11, we have an equation for the relationship between the ion and neutral densities,

$$n_i = n_n \frac{hm_i Q_{in}^{mt}}{2e^2 dw L' sin\theta cos\theta}. \tag{13}$$

In this equation Q_{in}^{mt} is the cross section of momentum transfer collisions between ions and neutrals in the sheet. This is the sum of the charge exchange and elastic scattering cross sections, and it is a function of the relative velocity between the ions and neutrals, or simply v_y itself.

We have now defined each reaction rate term in 6. Now, substituting each of these terms into equation 6, we have a second equation for the ion number density of the sheet,

$$n_i = n_a \frac{\nu^{enc}}{\nu^{rc} + \nu^l - \nu^{iz}}. \tag{14}$$

Note that the frequencies are functions of other frequencies or velocities and some are functions of n_i and T_e as well. The equation for each of the collision frequencies used in this paper is given in the appendix.

We can now iteratively solve for n_i and n_n from equations 13 and 14. In section VI we discuss the results of employing our model in this way to calculate the density, mass and impulse of the sheet. We will now discuss the method of calculating the velocity and mass of the wake.

IV. VELOCITY OF THE WAKE

When ions and neutrals from the sheet strike the cathode and enter the wake, they still have a velocity component in the x direction equal to the sheet velocity. However, since these particles are no longer in the sheet and do not carry current, they no longer feel the $j \times B$ force. It is clear from photographs that the wake as a whole moves more slowly than the sheet. Particles in the wake no doubt have a distribution of velocities in the x direction from 0 to v_{sh}. However, without employing a more sophisticated, time-dependent model, it is difficult to model the distribution of wake mass across this range of velocities. Instead we will assign to the wake an average velocity, and assume that the entire wake mass moves with this velocity.

We note that the time scale of collisions of ions in the wake is short compared to the time scale of the traversal down the electrodes [20],

$$\tau_{ii} = \frac{1}{\nu_{ii}} \approx 0.01 \mu s. \tag{15}$$

This means that the particles in the wake undergo many collisions that randomize their velocity (which was initially mostly x-directed). If the velocity is completely randomized, we would expect that the original energy (from v_{sh}, v_y, and v_{thi}) would be converted entirely into thermal energy, so that there

would be no net directed velocity. Also, if this was the case, particles in the wake would move quickly up towards the anode and the wake would soon cover the entire gap. This is not the observed behavior. From photographs, we observe that the wake ions tend to stay confined to a layer approximately half, or less, of the height of the electrode gap and continue moving in the x direction. This implies that there is a force that keeps the ions from drifting away from the cathode too far. Also, there must continue to be a directed component of the velocity, in addition to the thermal component. For the purposes of this model, we will make the approximation that the energy of the particles is split evenly between thermal energy in the y and z directions (v_{thy} and v_{thz}), and directed energy in the x direction (v_w).

$$E_0 = \frac{1}{2}m_i(v_{sh}^2 + v_y^2 + v_{thi}^2) = \frac{1}{2}m_i(v_w^2 + v_{thy}^2 + v_{thz}^2) \tag{16}$$

Setting the three velocities on the right side equal, under the approximation made above, we have:

$$v_w = \frac{1}{3}\left(v_{sh}^2 + v_y^2 + v_{thi}^2\right)^{\frac{1}{2}} \tag{17}$$

Here, we have defined the velocity of the wake in terms of the sheet velocity, cathode-directed velocity, and thermal velocity of ions in the sheet.

Neutral particles in the wake will receive, through collisions, velocity components away from the cathode. With no force to oppose them, some neutrals will drift away and be lost from the wake entirely. This will have two effects. One is that these neutrals will take energy away from the wake, reducing the effective v_w in the x direction that we are looking to calculate. The other effect is that this loss of neutrals will reduce the mass of the wake. We will make the assumption, however, that the neutral loss is negligible. Therefore, the mass and impulse of the wake will be overestimates.

V. MASS OF THE WAKE

The mass of the wake is straightforward to estimate, with a key assumption. Assuming that all of the mass that is not in the sheet is swept into the wake, we simply subtract the sheet mass from the total available mass in the accelerator channel,

$$M_w = m_a n_a h d l - M_{sh} = M_{av} - M_{sh} \tag{18}$$

where l is the length of the electrodes and we have defined M_{av} as the available mass.

This means that we are ignoring the potential loss of neutrals explained in the section above. Again, this will be an overestimate of the mass, and thus of the impulse as well. We know from photographs that this assumption is not entirely justified. When the current sheet reverses, a secondary or "re-strike" breakdown is observed. This second sheet must have a supply of gas left over to ionize. It might be possible, in fact, with a measurement of the number density of the "re-strike" sheet, to estimate how many neutrals lose forward momentum entirely and are left behind in the gap.

VI. RESULTS AND DISCUSSION

The first prediction of the model is the velocity of the sheet. Figure 3 shows the measured sheet velocity compared to the predicted snowplow velocity. The measurements and predictions are for argon and neon discharges over a range of pressures from 75 to 400 mTorr, and all at 4050 J of energy. The velocity measurements shown here are the average of only two magnetic field probe measurements each. The error bars shown in figure 3 and in all the following graphs are the standard deviations of the measurements.

We see in figure 3 that the velocity of the sheet is predicted fairly well by the snowplow velocity. We do see some discrepancy, however, with argon. At lower pressures, the measured velocity of the argon sheet is as much as 33% above the prediction. As expected, for both propellants the velocity decreases as the ambient pressure increases. This is because the drag from the ambient neutrals goes up while the $j \times B$ force remains the same (all discharges were performed with the same energy).

The goal of the mass balance section of the model is to predict the ion and neutral densities in the sheet. With knowledge of n_i and n_n in the sheet we can then calculate the sheet mass and impulse as well. In the simple model, the densities are uniform in the sheet, so the sheet mass is simply the product of the ion mass, ion density, and sheet volume. The impulse is the product of the sheet mass and velocity.

Before we continue, however, something must be said about the inputs to the model. The electron temperature is a necessary input, and the computed n_i is sensitive to the value of T_e. In equation 14, the frequencies ν^{rc} and ν^{iz} in the denominator both depend on the temperature, ν^{rc} strongly so. For an argon discharge at 75 mTorr, the electron temperature has been measured to be 2.4 ± 0.2 eV [1]. We have used this value in the model for argon at all
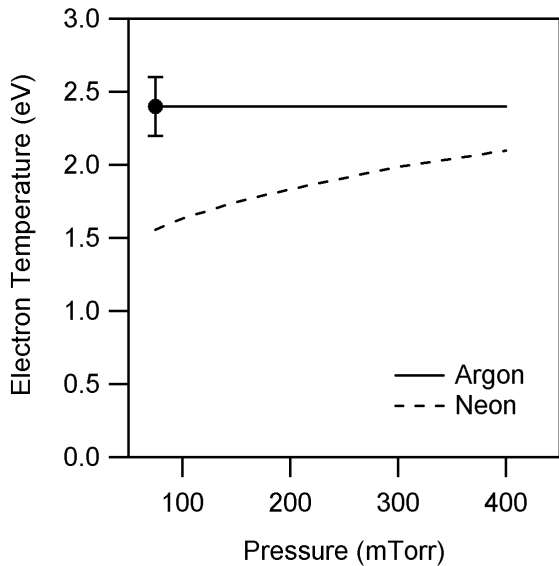
FIG. 15: Electron temperature versus pressure for argon and neon. The single data point is a measurement by Markusic in the same accelerator [1]. T_e was taken to be 2.4 eV for all argon discharges. T_e was a free parameter for neon discharges. The values shown were input to the model to give a good match between the experimental and modelled electron number densities.

pressures. For neon, however, using $T_e = 2.4$ eV does not give good results (the predicted n_i is about twice the measured n_i in this case). Instead, we will use T_e as a free parameter in the model for neon. Figure 15 shows the neon electron temperature as a function of pressure that was used to give good results for n_i.

We can see from figure 15 that the electron temperature implied by the model for neon is lower than that for argon. Also, while a single electron temperature works well for all pressures of argon, this is not the case for neon. The electron temperature increases with pressure for neon from about 1.5 to 2.0 eV. Although the right hand side of equation 14 is a complicated function of n_i and T_e, we can see to first order where this difference arises. The numerator in equation 14 is $n_a v_{sh}/w$. For argon, because of the linear dependence of w on v_{sh} (see figure 13), the ion number density is, to first order, dependent on n_a. In other words, the ion density increases with pressure without need to change the denominator through a changing temperature. For neon, however, w is constant and the product of n_a and v_{sh} goes like $n_a^{1/2}$. In this case, the first order effect on the ion number density is not as strong. A rising T_e with pressure is required to decrease the recombina-

tion frequency and increase the ionization frequency, thus increasing n_i further with pressure.

We will not attempt a full thermodynamic explanation for why the electron temperature should be lower in the neon sheet than the argon sheet. One possible reason, however, is that more energy is required to ionize neon than argon, thus leaving excess energy to electrons in the argon plasma. With these inputs for electron temperature explained, we can now compare the results of the mass balance section of the model, beginning with the ion number density.

In figure 4, we compare the measured electron number density peaks to the predicted ion number density. For argon, the measurements are the averages of ten interferometry measurements, and for neon only two.

The electron number density (figure 4) is matched well by the model for both argon and neon. For neon, the electron temperatures shown in figure 15 were chosen to make this comparison fit well. For argon, however, the electron temperature used was a measured one, so there is no free parameter. We see that for both propellants, there is an increase in peak electron number density with pressure. The peak electron number density for argon is approximately two times greater than that of neon.

Next, we compare the predicted and measured masses of the ions in the sheet. Figure 5 shows this comparison for argon and neon. The mass is greater for argon than for neon, as might be expected considering that the argon ion is about twice the mass of the neon ion. The trends for the two propellants are different, however. The argon sheet mass stays approximately constant with pressure, but the neon sheet mass increases. This is because while the ion density increases with pressure for both propellants, the width of the argon sheet clearly decreases, offsetting the trend, but the width of the neon sheet does not. The widths used in the model were the experimentally measured widths, therefore it is not surprising that the mass predictions match well to the experimental data.

The impulse of the sheet ions is now compared to the calculated sheet ion impulse. Figure 7 shows this comparison for argon and neon. The impulse is the product of the mass of the sheet ions and the sheet velocity. Again, the mass of the sheet neutrals is not included here in the measurements or predictions. The impulse for argon is seen to decrease with pressure. This is due to the constant mass being multiplied by a velocity that decreases with pressure (see figure 3). The model under-predicts the argon impulse at lower pressures because of the previously mentioned under-prediction of the velocity at lower pressures. For neon, the impulse remains

fairly constant, perhaps with a slight upward trend versus pressure. This is due to the sheet mass that increases with pressure being offset by a velocity that decreases with pressure.

In figures 9 and 10 the dashed lines represent the total impulse of the sheet for argon and neon, respectively. These predictions are similar to the impulses of the sheet ions reported above in figure 7. This is because the sheet is overwhelmingly composed of ions, so the neutrals add very little to the mass and impulse.

The dotted lines in figures 9 and 10 show the impulse of the wake. The wake impulse increases with pressure. This is to be expected because discharges at higher pressures have more propellant mass available to them. Since the mass of the sheet does not increase in proportion to the available mass, a lower percentage of the available mass is included in the sheet at higher pressures. This leaves more mass available to the wake. This increase in wake mass with pressure is sufficient to overcome the decrease in wake velocity with pressure (due to the same trend for sheet velocity). The wake impulse goes from being a small percentage of the sheet impulse at 75 mTorr to equal to the sheet impulse for neon at 400 mTorr and almost twice the sheet impulse for argon at 400 mTorr.

Adding the wake and sheet impulses, we predict the total impulse of the device and compare it to the total impulse measured with a momentum plate. In figures 9 and 10, the total impulse prediction is shown with a solid line and the measurements are shown with data points.

We see in this comparison that the prediction falls below the measurement, especially for neon and especially at lower pressures. One possible explanation for the momentum plate measurements being higher than the predicted impulse is the following. The electrode length and the time of the current pulse are constant in our experiments. At approximately 25 μs, the current (which had been relatively constant) begins to decrease, and by 30 μs, it reverses. This means that fast-moving sheets reach the end of the electrodes before the current reverses, while slow moving sheets do not. In fact, in our experiments, only argon current sheets at 300 and 400 mTorr are slow enough not to reach the end of the electrodes by 25 μs (photographs of the end of the electrodes with an argon discharge at 300 mTorr show it reaches the end of the electrodes at about 27 μs). For all other cases, current is still being supplied to the sheet when it reaches the end of the electrodes. When this happens, the sheet balloons out instead of disconnecting from the electrodes. Thus, there exists a quasi-steady blowing phase in those cases, which

can add impulse [21, 22]. For example, the wake particles which had lagged the sheet may now catch up to it, feel the $j \times B$ force, and be re-accelerated.

The fastest discharges modelled here are the neon discharges at low pressures (see figure 3), therefore these discharges would have the highest blowing component of the impulse. This is consistent with the largest disparity between the measurements and model being at low pressures, and for the lighter gas, neon. Also, the prediction is close to the data in the case of argon at higher pressures, when there is little or no blowing component of the impulse expected.

For both argon and neon, the modelled total impulse rises with pressure. This trend indicates a surprising result. The predicted total impulse is higher in the case where a larger percentage of the mass is in the wake. However, we notice that the higher pressure discharges use many times the mass of propellant to achieve only slightly higher impulse. This indicates that the specific impulse will decrease with pressure. Specific impulse is the total impulse divided by the propellant weight,

$$I_{sp} = \frac{I_{total}}{M_{av}g_0}. \qquad (19)$$

where M_{av} is the total available mass of propellant in the accelerator (in our case, this is the mass of the sheet and wake together). Figure 16 shows the measured and modelled specific impulses calculated from equation 19.

We see that while increased pressure causes the total impulse to increase, it causes the specific impulse to decrease. This is not surprising, considering that the sheet velocity decreases with pressure.

Another measure of the performance of the device is acceleration efficiency,

$$\eta = \frac{I_{total}^2}{2M_{av}E}, \qquad (20)$$

where, E is the energy per pulse. In all the data presented here, $E = 4050$ J was used. Figure 17 shows the efficiency versus pressure for argon and neon, again both from experimental measurements and from our analytical model.

In figures 16 and 17 the experimental values of specific impulse and efficiency are greater than the predicted values. This is due to the increased impulse in the experiments from the blowing mode, as discussed above. Regardless, both the experiments and the model show the same trends. When the pressure is increased, the wake impulse constitutes a higher percentage of the total impulse, indicating
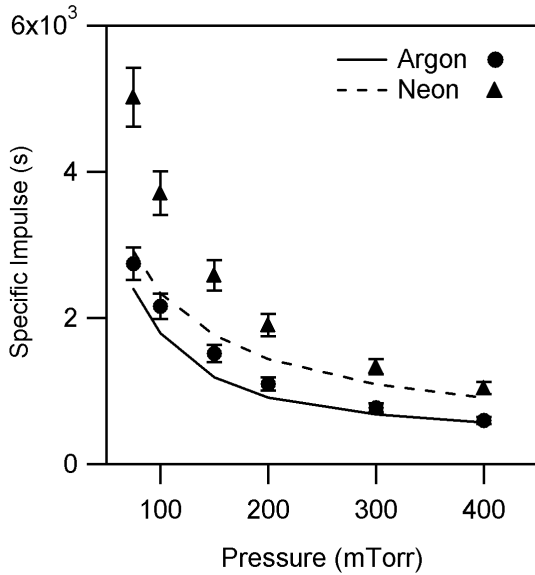
FIG. 16: Specific impulse versus pressure for argon and neon calculated from both the momentum plate measurements and the modelled total impulse.
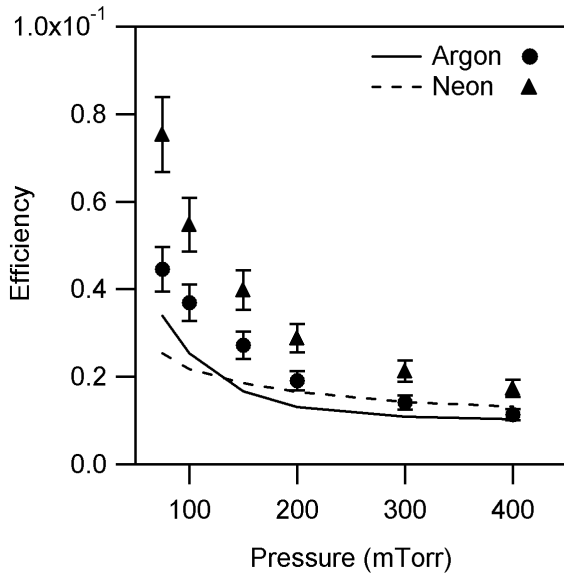

FIG. 17: Efficiency versus pressure for argon and neon calculated from both the momentum plate measurements and the modelled total impulse.

greater plasma leakage. This causes the total impulse to increase slightly, but the specific impulse and efficiency decrease. Therefore plasma leakage causes a degradation of performance of the device.

VII. CONCLUSIONS

We have described experimental measurements of the velocity, electron number density, mass and impulse of the current sheet in a parallel plate pulsed electromagnetic accelerator. The total impulse of the discharge, including the momentum of both the sheet and wake have also been measured with a momentum plate. All of these data are presented for argon and neon discharges over the pressure range of $75 - 400$ mTorr.

An analytical model of the propagation phase of the discharge has been presented. We used a force balance to model the current sheet velocity, and a mass balance to model the ion number density, and hence the mass, of the current sheet. The mass and velocity of the plasma wake have also been estimated. For neon, the electron temperature is used as a free parameter in the model, whereas for argon there is no free parameter.

The goal of this study has been to determine the impact of the plasma leakage phenomenon by studying the division of impulse between the sheet and the wake. We find that the impulse of the wake increases from about 10% to nearly 67% of the total impulse in argon discharges over the range of $75 - 400$ mTorr, and from 20% to 50% for neon. We also find that the total impulse of the device increases with increasing propellant fill pressure for both argon and neon. The specific impulse and efficiency, however, decrease. Plasma leakage has a detrimental effect on the performance of the electromagnetic pulsed plasma thruster.

VIII. APPENDIX

The collision frequencies and cross sections used in this model are given here in detail.

Electron-Neutral Ionization Collision Frequency

$$\nu_{en}^{iz} = n_n \left(\frac{2}{m_{en}} \right)^{\frac{1}{2}} \int_0^\infty \left(\frac{2\epsilon_{en}}{\pi^{\frac{1}{2}} \left(kT_e \right)^{\frac{3}{2}}} \right) Q_{en}^{iz} e^{\frac{-\epsilon_{en}}{kT_e}} \, d\epsilon_{en}$$

(21)

Radiative Recombination Frequency [23]

$$\nu_{ei}^{rr} = 2.1622 * 10^{-33} \frac{n_e}{\left(kT_e \right)^{\frac{3}{4}}}$$

(22)

Three Body Recombination Frequency [23]

$$\nu_{eei}^{tb} = 2.30784 * 10^{-123} \frac{n_e^2}{\left(kT_e \right)^{\frac{9}{2}}}$$

(23)

13

Ion-Ion Collision Frequency [20]

$$\nu_{ii} = \frac{n_i Z^4 e^4 ln(\Lambda)}{12\pi^{\frac{3}{2}} \epsilon_0^2 m_i^{\frac{1}{2}} (kT_i)^{\frac{3}{2}}} \tag{24}$$

For cross sections, the following fits to experimental data were used:

Electron-Neutral Ionization Cross Section [24]

$$Q_{en}^{iz}|_{Argon} = -2.779 * 10^{-20} + 1.1 * 10^{-2}\epsilon \tag{25}$$

$$Q_{en}^{iz}|_{Neon} = -3.475 * 10^{-21} + 1.0 * 10^{-3}\epsilon \tag{26}$$

Ion-Neutral Ionization Cross Section [25]

$$Q_{in}^{iz}|_{Argon} = 2.8 * 10^{-20} - 2.9 * 10^{-20} e^{\frac{-\epsilon}{8.4*10^{-17}J}} \tag{27}$$

$$Q_{in}^{iz}|_{Neon} = 3.5 * 10^{-20} - 3.75 * 10^{-20} e^{\frac{\epsilon}{1.8*10^{-16}J}} \tag{28}$$

Ion-Neutral Charge Exchange Cross Section [23]

$$Q_{in}^{cx}|_{Argon} = 5.8 * 10^{-19} - 3.8 * 10^{-20} ln\left(\frac{\epsilon}{1.6022 * 10^{-19}J}\right) \tag{29}$$

$$Q_{in}^{cx}|_{Neon} = 3.3 * 10^{-19} - 3.8 * 10^{-20} ln\left(\frac{\epsilon}{1.6022 * 10^{-19}J}\right) \tag{30}$$

Ion-Neutral Elastic Scattering Cross Section [23]

$$Q_{in}^{es}|_{Argon} = 4.8 * 10^{-19} - 3.8 * 10^{-20} ln\left(\frac{\epsilon}{1.6022 * 10^{-19}J}\right) \tag{31}$$

$$Q_{in}^{es}|_{Neon} = 2.4 * 10^{-19} - 3.8 * 10^{-20} ln\left(\frac{\epsilon}{1.6022 * 10^{-19}J}\right) \tag{32}$$

[1] T.E. Markusic. *Current Sheet Canting in Pulsed Electromagnetic Accelerators*. PhD thesis, Princeton University, 2002.

[2] T.E. Markusic and E.Y. Choueiri. Phenomenological model of current sheet canting in pulsed electromagnetic accelerators. In 28th *International Electric Propulsion Conference*, Toulouse, France, March 17-24 2003. IEPC 2003-0293.

[3] T.E. Markusic, E.Y. Choueiri, and J.W. Berkery. Measurements of current sheet canting in a pulsed electromagnetic accelerator. *accepted for publication to Physics of Plamas*, 2004.

[4] J.W. Berkery and E.Y. Choueiri. Characterization of current sheet evolution in a pulsed electromagnetic accelerator. In 28th *International Electric Propulsion Conference*, Toulouse, France, March 17-24 2003. IEPC 2003-0307.

[5] J.W. Berkery. Movies of magnetic and interferometric experimental contours in a parallel-plate gas-fed pulsed plasma thruster discharge. http://www.princeton.edu/~eppdyl/personnel/berkery.html.

[6] F.J. Fishman and H. Petschek. Flow model for large radius-ratio magnetic annular shock-tube operation. *Physics of Fluids*, 5:632–633, 1962.

[7] R.H. Lovberg. The measurement of plasma density in a rail accelerator by means of schlieren photography. *IEEE Transactions on Nuclear Science*, 11:187–198, 1964.

[8] J.R. MacLelland, A.S.V. MacKenzie, and J. Irving. Schlieren photography of rail-tube plasmas. *Physics of Fluids*, 9:1613–1615, 1966.

[9] T.E. Markusic and E.Y. Choueiri. Photographic, magnetic, and interferometric measurements of current sheet canting in a pulsed electromagnetic accelerator. In 37rd *Joint Propulsion Conference*, Salt Lake City, Utah, July 8-11 2001. AIAA 2001-3896.

[10] D.M. Wetstone. Coaxial plasmoid source of small aspect ratio. *Physics of Fluids*, 5(8):981–987, 1962.

[11] S.F. Goncharov, P.P. Pashinin, R.V. Serov, and V.P. Yanovsky. Hollow ballistic pendulum for plasma momentum measurements. *Review of Scientific Instruments*, 59(5):709–711, 1988.

[12] J. Marshall. Performance of a hydromagnetic plasma gun. *Physics of Fluids*, 3(1):134–136, 1960.

[13] A. Andrew and J.P. Fitzpatrick. Velocity and impulse of an accelerated plasma. *Physics of Fluids*, 1960.

[14] J. Grun and B.H. Ripin. Ballistic pendula for measuring the momentum of a laser-produced plasma. *Review of Scientific Instruments*, 53(12):1878–1881, 1982.

[15] J. Marshall. Hydromagnetic plasma gun. In S.W. Kash, editor, *Plasma Acceleration*. Stanford University Press, 1960.

[16] W.L. Starr and J.T. Naff. Acceleration of metal-derived plasmas. In S.W. Kash, editor, *Plasma Acceleration*. Stanford University Press, 1960.

[17] I. Kohlberg and W.O. Coburn. A solution for three dimensional rail gun current distribution and electromagnetic fields of a rail launcher. *IEEE Transactions on Magnetics*, 31(1):628–633, 1995.

[18] W.R. Ellis and R.G. Jahn. Ion density and current distributions in a propogating current sheet, determined by microwave reflection technique. *Journal of Plasma Physics*, 3(2):189–213, 1969.

[19] R.B. Johansson. Current sheet tilt in a radial magnetic shock tube. *Physics of Fluids*, 8(5):866–871, 1964.

[20] R.J. Goldston and P.H. Rutherford. *Introduction to Plasma Physics*. IOP Publishing, 1995.

[21] A.C. Eckbreth, K.E. Clark, and R.G. Jahn. Current pattern stabilization in pulsed plasma accelerators. *AIAA Journal*, 6(11):2125–2132, 1968.

[22] A.C. Eckbreth and R.G. Jahn. Current pattern and gas flow stabilization in pulsed plasma accelerators.

AIAA Journal, 8(1):138–143, 1970.

[23] Y.P. Raizer. *Gas Discharge Physics*. Springer-Verlag, 1991.

[24] S.C. Brown. *Basic Data of Plasma Physics*. AIP Press, 1994.

[25] J.A. Kunc and W.H. Soon. Analytical ionization cross sections for atomic collisions. *Journal of Chemical Physics*, 8(15):5738–5751, 1991.